RESEARCH ARTICLE | JANUARY 28 2025

Efficient methods for extracting superconducting resonator loss in the single-photon regime ⓈⒸⒾ Ⓕ

Cliff Chen ✉ ⓘ ; David Perello ⓘ ; Shahriar Aghaeimeibodi ⓘ ; Guillaume Marcaud ⓘ ; Ignace Jarrige ⓘ ;
Hanho Lee ⓘ ; Warren Fon ⓘ ; Matt Matheny ⓘ ; Jiansong Gao ⓘ

Check for updates

🌐 View Online   ➡ Export Citation

Articles You May Be Interested In

Ironing out kinks in quantum computing

Scilight (January 2025)

Lumped element granular aluminum resonators with high kinetic inductances

AIP Advances (June 2021)

Acceleration of ferromagnetic resonance measurements by Bayesian experimental design

Rev. Sci. Instrum. (October 2024)

Efficient methods for extracting superconducting resonator loss in the single-photon regime

Cliff Chen,[a] David Perello, Shahriar Aghaeimeibodi, Guillaume Marcaud, Ignace Jarrige, Hanho Lee, Warren Fon, Matt Matheny, and Jiansong Gao

AFFILIATIONS

AWS Center for Quantum Computing, Pasadena, California 91106, USA

[a]Author to whom correspondence should be addressed: clfchen@amazon.com

ABSTRACT

Superconducting micro-resonators have application in sensors and quantum computing. Measurement of the resonator internal loss in the single-photon regime is a common tool to study the origins of dissipation, noise, and decoherence in quantum circuits, as well as characterization of materials used for quantum devices. However, such measurements are challenging and time-consuming with large uncertainties due to the poor signal-to-noise ratio when measured at single-photon power levels. We developed methods to extract a subset of the resonator fitting parameters at high power and fix them in the analysis of low power data, which reduce the parameter space in the regression analysis. By comparing the analysis with and without partial extraction, we show that these methods reduce the uncertainty of the results, while improving the robustness and efficiency of the loss measurement.

I. INTRODUCTION

Superconducting resonators are essential circuit elements in microwave photonics and quantum computing applications.[1] The most popular superconducting qubit design, the transmon qubit,[2,3] uses a Josephson junction as a non-linear inductor in an LC tank circuit to form an anharmonic oscillator with the ground and first excited states comprising the qubit. It is known that a large fraction of the loss is associated with the electric fields of the qubit penetrating the shunt capacitor and the ground plane outside the junction.[4] The primary benefit of using resonators as opposed to qubits to extract loss is the general ease of design and fabrication. For example, planar linear resonator fabrication can be simplified to a one-layer deposition and patterning process without a junction, bandage, or integration layer.[5]

At millikelvin temperatures and single-photon excitation powers, superconducting resonator quality factors are ultimately limited by two-level systems (TLSs) residing in the amorphous dielectric materials at the interfaces between the air, superconductor, and substrate.[6,7] At high power, TLSs are saturated[8,9] and become less saturated as power decreases leading to a power-dependent resonator internal quality factor Q_i (or internal loss $1/Q_i$). When measured as a function of photon number $\langle n_{ph} \rangle$ or internal field strength, this power-dependent relationship can be exploited to differentiate TLS-related loss from power-independent losses due to quasiparticles, radiation, trapped flux, etc.[10–13]

The power-dependent losses are commonly measured using a vector network analyzer (VNA) to obtain a set of scattering parameters, $S_{21}(f)$, as a function of $\langle n_{ph} \rangle$ within a few linewidths around the resonance frequency f_r. The quality factor and other resonator parameters can be extracted from independent fits to the complex S_{21} for each power. Determining the TLS-induced loss this way often requires $\langle n_{ph} \rangle \lesssim 1$ so one must decrease the VNA power to very low levels. In this regime, the measurement signal-to-noise ratio (SNR) is poor and limited by the cryogenic amplifier noise in typical setups. The low SNR reduces the fit quality and often produces unreliable Q_i values with large uncertainties.[14] To increase SNR, one must inevitably increase acquisition time, but this, in turn, makes the measurement susceptible to long term drift from TLS and the amplifiers. For these reasons, accurately determining resonator Q_i at single-photon power levels remains challenging and time consuming.

In this paper, we address this challenge by improving the measurement and data analysis methodologies. Instead of fitting parameters independently at each power as is conventionally done,

our strategy is to extract a subset of the resonator fitting parameters (such as the coupling Q_c and the impedance mismatch angle ϕ) from high power data and fix these parameters in the analysis of low power data. We use this method of partial parameter extraction to analyze experimental data acquired from Al and Nb resonators and show that great improvements have been achieved in terms of accuracy and robustness of the results.

II. REVIEW OF THE CONVENTIONAL METHOD

Resonator measurements are often frequency multiplexed in a signal chain by "hanging" individual resonators off a common feedline as shown in Fig. 1(a). The corresponding circuit diagram is shown in Fig. 1(b). In this configuration, $S_{21}(f)$ is described by

$$S_{21}(f) = e^{-j2\pi f\tau}z(f) = e^{-j2\pi f\tau}a\,e^{j\alpha}\left[1 - \frac{Q_l/Q_c\,e^{j\phi}}{1 + 2jQ_l\left(\frac{f-f_r}{f_r}\right)}\right], \quad (1)$$

where τ is the cable delay, $a\,e^{j\alpha}$ is the off resonance point or signal background, ϕ is the on-chip impedance mismatch angle, and f_r,

Q_c, Q_l are the resonance frequency, coupling quality factor and loaded quality factor, respectively.[15] For clarity of notation, we represent the complex scattering parameter without the cable delay term ($e^{-j2\pi f\tau}$) by the variable z hereafter.

Estimating the parameter values in this equation from experimental data is a non-linear over-defined multi-parameter fitting problem that is sensitive to initial parameter estimates. Instead of directly carrying out the multi-parameter fitting, a common practice is to decompose the original problem into a series of analyses which focus on extracting a few parameters at a time. First, the cable delay is removed which is followed by a circle fit to determine the center and radius of the resonance circle. An additional phase unwrapping and fit determines the parameters Q_l, f_r, Q_c, and ϕ along with the off resonance point $z_\infty = a\,e^{j\alpha}$. This multi-step fitting procedure is explained in more detail in Fig. 1 as well as in Gao.[16] Once this procedure is done, one may report the obtained parameters as the final values or use them as initial values in a multi-parameter fit to Eq. (1) to refine them further. At this point, one may extract the internal quality factor Q_i. It has been shown using both a circuit model[17] and a network model[18] that Q_i can be
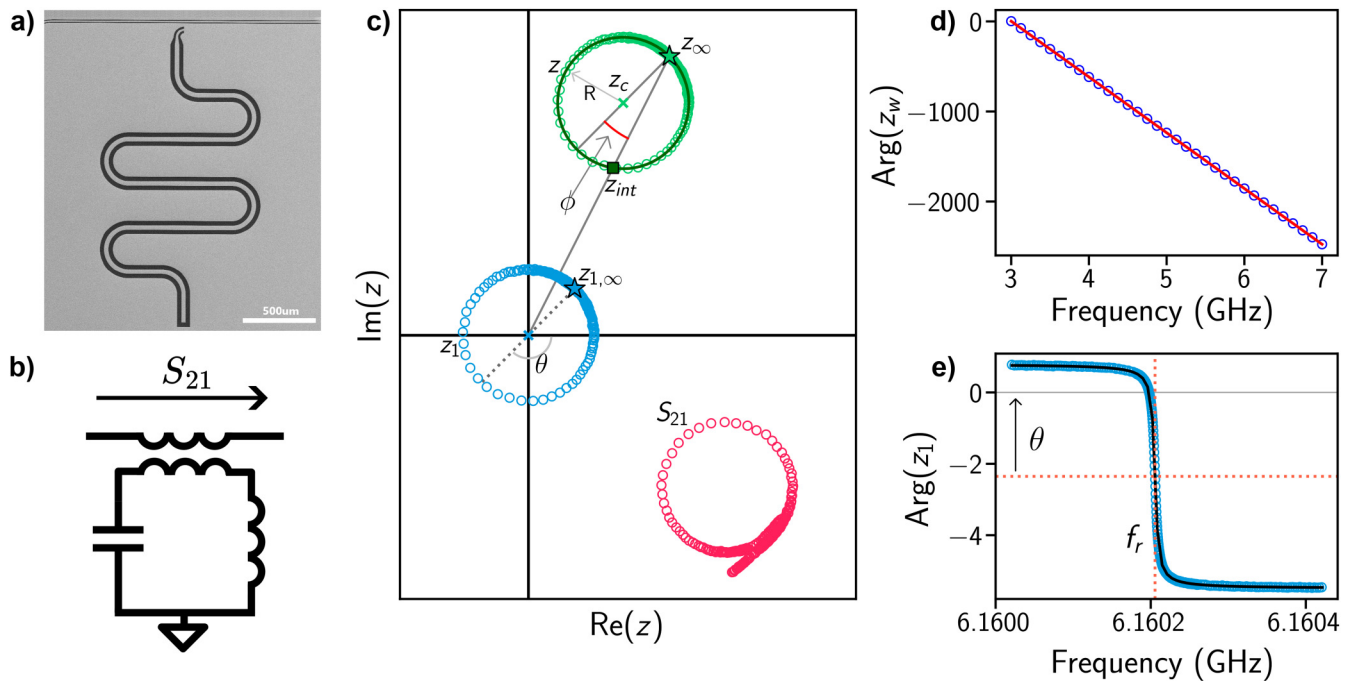
FIG. 1. Conventional multi-step fitting procedure. (a) Scanning electron micrograph of a $\lambda/4$ coplanar waveguide (CPW) resonator in the hanger configuration inductively coupled to a transmission line. (b) The lumped element circuit diagram representing the resonator featured in (a). (c) The raw data S_{21} are plotted in red. The cable delay term $e^{-j2\pi f\tau}$ introduces a frequency dependent rotation that causes the raw data to wrap onto itself. The cable delay τ is determined by a linear fit to the phase of a wide frequency S_{21} sweep shown in (d). Removing the cable delay-induced phase gives the unwrapped data z (green): $z = S_{21}/e^{-j2\pi f\tau}$. Next, z is fit to a circle (solid line) to determine the radius R and circle center z_c (green $\times$). This allows the data to be translated to the origin to obtain the centered data z_1 (blue): $z_1 = z - z_c$. The phase angle of the complex z_1 is fit to a nonlinear model $\mathrm{Arg}(z_1) = 2\arctan(2Q_l(1 - f/f_r)) - \theta$ to obtain Q_l, f_r and θ. The coupling Q_c is found as $Q_c = Q_l|z_\infty|/2R$ and the impedance mismatch angle ϕ is found as $\phi = \mathrm{Arg}(z_\infty) + \theta - \pi$. (d) The unwrapped phase of a broadband frequency sweep z_w plotted as a function of frequency. A linear fit (red line) to $\mathrm{Arg}(z_w) = -2\pi f\tau + b$ (b is some constant) determines the cable delay $\tau = 107.6 \pm 8.6 \times 10^{-5}$ ns. Note that τ is the time (typically 50–300 ns) required for a signal to make the roundtrip from port 1 to port 2 of the VNA and includes the delay on the chip. (e) The phase angle of z_1 vs frequency. A nonlinear fit (black line) to an arctan function determines Q_l, f_r and θ.

retrieved from the simple geometric relationship,

$$\frac{Q_i}{Q_l} = \frac{|z_{int}|}{|z_\infty|} = \frac{|z_\infty| - 2R\cos\phi}{|z_\infty|}, \quad (2)$$

where z_{int} is the intersection point of the resonance circle and the line from the origin to z_∞ [green square in Fig. 1(c)]. These models have also found that a non-zero ϕ rises due to discontinuities or unmatched impedances in the circuit. This modifies the effective Q_c' of the resonant circuit to be

$$\frac{1}{Q_i} = \frac{1}{Q_l} - \frac{1}{Q_c'}, \quad Q_c' = \frac{Q_c}{\cos\phi}. \quad (3)$$

Equation (3) along with the multi-parameter fitting procedure constitutes the diameter correction method (DCM).[17]

III. UPDATING THE DCM WITH CONSTRAINED PARAMETERS OBTAINED AT HIGH POWER

The diameter correction method works well for obtaining resonator parameters at large microwave powers but begins to produce poor fits at lower powers where the SNR is low. We introduce an updated version of DCM called parameter-constrained DCM (PC-DCM) that improves the quality and reliability of the fitting procedures at all powers. The main motivation behind PC-DCM is that many parameters listed in Eq. (1) are constant for any number of photons as long as the system response is linear (free from nonlinear effects such as amplifier saturation and non-linear kinetic inductance). These parameters can be determined with much higher accuracy at higher powers, and then reused to fit data at lower powers. Parameters such as ϕ, a, α, τ describe circuit properties of the signal chain rather than the resonator itself. Meanwhile, Q_c is fixed by design. The two remaining parameters, f_r and Q_i, can depend on power (e.g., due to TLS saturation and nonlinear kinetic inductance effect[19]). For low power resonator loss measurements on resonators with a low kinetic inductance fraction, the power dependence of f_r is typically much weaker than Q_i.[16]

Another update in PC-DCM to improve the fitting efficiency and robustness is to reduce the frequency span of the S_{21} measurement to within one linewidth of the resonance frequency while taking data at low power. We do this for the following reason. By taking the derivative of Eq. (1), one can derive

$$\left|\frac{\delta S_{21}}{\delta 1/Q_i}\right| = \frac{|z_\infty|/Q_c}{\left(\frac{1}{Q_l}\right)^2 + \left(2\frac{f-f_r}{f_r}\right)^2}, \quad (4)$$

which is a Lorentzian function of f peaked at $f = f_r$. This implies that the S_{21} measurement is most sensitive to a change in $1/Q_i$ on resonance. Therefore, in order to obtain the best estimate of $1/Q_i$, it is always more favorable to include data closer to the resonance frequency. Data taken further off resonance only serve to further constrain the parameters associated with the signal chain (ϕ, a, α) rather than the power-dependent resonator parameters Q_i and f_r. Off resonance data can also influence the fitting algorithm to converge to a sub-optimal fit if it is not weighted properly.
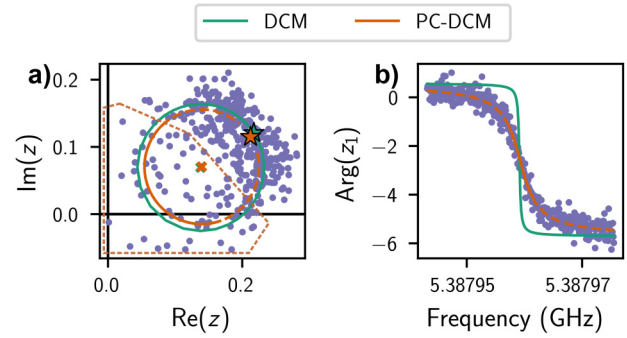
FIG. 2. A fitting example using DCM and PC-DCM. (a) Unwrapped data z from a 100 nm Al resonator taken at ~ 2 photons spanning 8 linewidths centered at f_r is plotted in purple. A subset of the points within the red dashed box spanned 1 linewidth. The full data set (purple) is fit using DCM while the subset (red dashed box) is fit using PC-DCM. The constrained parameters Q_c, ϕ, z_∞ in the PC-DCM fit are predetermined from the DCM fittings to the data measured at 10^5 photons. Off resonance points are marked by "★." (b) The unwrapped phase of the centered data z_1 vs frequency. In both a and b, the solid lines indicate the fits to the data using the DCM and the PC-DCM. The red dashed line is the PC-DCM fit extrapolated to the rest of the data.

The PC-DCM procedure has four steps. First, accurately determine the cable delay τ from a wideband frequency sweep (same as in DCM). Second, use DCM to fit all parameters using high power data. The values obtained from the fit, such as a, α, ϕ and Q_c, are now treated as constant values just like τ. Third, perform a parameter-constrained circle fit, phase fit and an optional refining fit on the lower power data using the previously determined $a, \alpha, \phi, Q_c, \tau$ as constant values. This reduces the fitting problem in Eq. (1) down to a two-parameter fit for f_r and Q_l. Finally, extract Q_i from Eq. (3).

We measured a 100 nm Al resonator patterned on a Si substrate [Fig. 1(a)], to show how PC-DCM can improve the fitting quality over DCM. Figure 2(a) shows the measured z-data of the resonator at $\langle n_{ph}\rangle \sim 2$. This data set spanned 8 linewidths is fit using DCM (green circle). A subset of the data spanning 1 linewidth enclosed by the dashed box is fit using PC-DCM (red circle) with the constrained parameters z_∞, Q_c, and ϕ predetermined at a higher power. We extract $1/Q_i$ to be $7.5 \pm 3.2 \times 10^{-8}$ for DCM and $2.5 \pm 0.23 \times 10^{-7}$ for PC-DCM. The reason for this discrepancy can be traced to back to the phase fit in Fig. 2(b) which shows that the DCM fit converged to a sub-optimal result. The corresponding reduced χ_ν^2 for the DCM fit is 5.01, whereas it is 1.07 for the PC-DCM fit. This highlights the importance of constraining the parameter space to improve fitting reliability in the presence of noise and reduce the number of erroneous fits.

IV. CONFORMAL MAPPING WITH CONSTRAINED PARAMETERS

In this section, we describe a new method for analyzing resonators based on a conformal map of the S_{21} data. We show how the unwrapped data $z(f)$ can be mapped from the z-plane to a new w_2-plane with $w_2 = 1/Q_i + 2\delta f/f_r$. Conformal mapping is a

TABLE I. Table of variable definitions and relationships.

Definition	Variable	Relationship
Raw S_{21} data	S_{21}	
Cable delay removed	z	$z = S_{21} e^{j2\pi f\tau}$
Centered data	z_1	$z_1 = z - z_c$
Normalized data	z_2	$z_2 = z/z_\infty$
Inverted data	w	$w = (1 - z_2)^{-1}$
Rotated, inverted data	w_1	$w_1 = we^{j\phi}$
Conformally mapped data	w_2	$w_2 = (w_1 - \cos\phi)/Q_c$

powerful mathematical tool that has broad applications in microwave engineering.[20] It is often used to map orthogonal curvilinear coordinates into cartesian coordinates. In our method, the two orthogonal quadratures, often referred to as the frequency quadrature (tangential to the circle) and the dissipation quadrature (perpendicular to circle),[21] are mapped to the imaginary part and real part in the new w_2-plane, respectively. This is possible because Eq. (1) has the general form of a bilinear (or Mobius) transformation:[22] $\xi = (a\eta + b)/(c\eta + d)$, which is a special class of conformal maps that map lines and circles in the η-plane into lines and circles in the ξ-plane. The two following subsections illustrate how to use this new fitting method to determine resonator parameters at high power as well as establish the conformal map to analyze data taken at low power.

A. Fitting procedures to establish the conformal map at high power

Here, we walk through the steps to develop the conformal map; a summary of the variable relationships can be found in Table I. Figure 3(a) shows the normalized data $z_2(f)$ measured on a

100 nm Al resonator at $\langle n_{\mathrm{ph}}\rangle \gg 1$ plotted as the dark circle. The normalized data are, defined as

$$z_2 = \frac{z}{z_\infty} = 1 - \frac{Q_l/Q_c\, e^{j\phi}}{1 + 2jQ_l\delta f/f_r}, \tag{5}$$

where $\delta f = f - f_r$ is the detuning and z_∞ is the aforementioned off resonance point. The transformation

$$w = \frac{1}{1 - z_2} = \frac{Q_c}{Q_l}\, e^{-j\phi}(1 + 2jQ_l\delta f/f_r), \tag{6}$$

transforms the resonance circle in the z_2-plane into a straight line in the w-plane. This is apparent from Eq. (6) where $1 + 2jQ_l\delta f/f_r$ represents a vertical line and $e^{-j\phi}$ represents a rotation by an angle ϕ, as shown in Fig. 3(a). The angle ϕ is determined from a line fit of the real and imaginary parts of w as

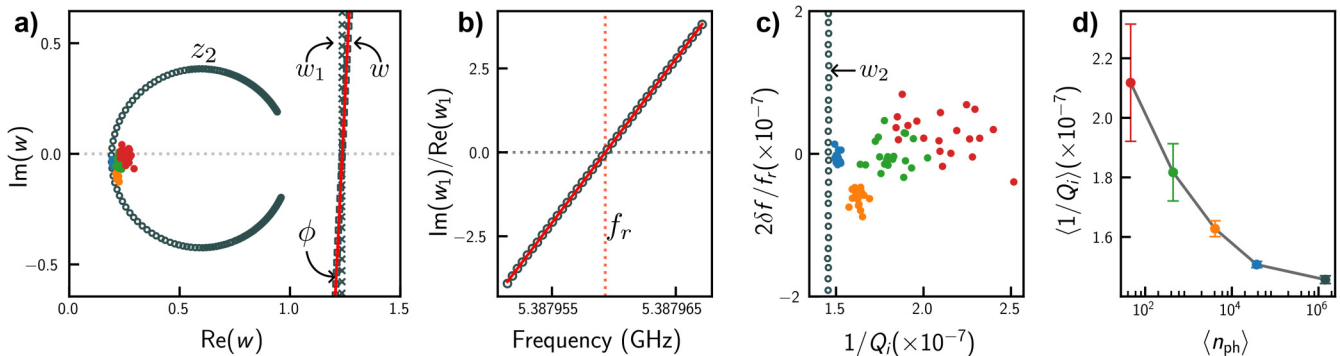$$\mathrm{Re}[w] = \tan\phi\,\mathrm{Im}[w] + b, \tag{7}$$

where b is some offset. The fitted value of ϕ is then used to rotate the line back to the following vertical line, such that

$$w_1 = w\, e^{j\phi} = \frac{Q_c}{Q_l} + 2jQ_c\delta f/f_r. \tag{8}$$

Given Eq. (8), we can find f_r and Q_l from a second linear fit of $\mathrm{Im}[w_1]/\mathrm{Re}[w_1]$ against f as shown in Fig. 3(b),

$$\frac{\mathrm{Im}[w_1]}{\mathrm{Re}[w_1]} = 2Q_l\delta f/f_r = 2Q_l\frac{f - f_r}{f_r}, \tag{9}$$

such that Q_c can be found from $Q_c = \mathrm{Re}[w_1]Q_l$.

FIG. 3. Conformal mapping method to fit resonator parameters and determine $1/Q_i$ step by step. (a) The unwrapped data z measured at high power on a 100 nm Al resonator are normalized to z_2 (dark circle). The map $w = (1 - z_2)^{-1}$ turns the resonance circle into a straight line. Next, the w data are further rotated to a vertical line to obtain $w_1 = w\, e^{j\phi}$, where ϕ is determined by finding the slope of the w-line from a linear fit (red line). The colored dots corresponds to time dependent data taken at a single frequency at different photon numbers. (b) Plot of the ratio $\mathrm{Im}[w_1]/\mathrm{Re}[w_1]$ as a function of frequency to determine Q_l, f_r, and Q_c. The red line indicates the best linear fit. (c) The w_1-line is further scaled and translated to obtain $w_2 = (w_1 - \cos\phi)/Q_c = 1/Q_i + 2\delta f/f_r$ (open circles). A simple average of $\mathrm{Re}[w_2]$ yields $1/Q_i$, which concludes the fitting procedure for data at $\langle n_{\mathrm{ph}}\rangle \gg 1$ and establishes the conformal map from z to w_2. The time-dependent single-frequency transmission data $z(t)$ measured at different $\langle n_{\mathrm{ph}}\rangle$ [colored dots inside the circle in (a)] are directly mapped to $w_2(t)$ [colored dots in (c)]. (d) A plot of $1/Q_i$ vs $\langle n_{\mathrm{ph}}\rangle$ generated from the mean of $\mathrm{Re}[w_2]$ of the data points for each power in (c) with the error bar calculated from the standard error of the mean. Here we only show data for five sparsely spaced n_{ph} levels for clarity of the plots. Full power sweeps down to single photon level will be discussed in the next section.

A re-scaling and translation of w_1 gives the final expression for w_2 as

$$w_2 = \frac{w_1 - \cos\phi}{Q_c} = \frac{1}{Q_i} + 2j\delta f/f_r, \quad (10)$$

where we have used the relationship in Eq. (3). The final transformed data are shown as open circles in Fig. 3(c). Now, $1/Q_i$ is reported by a simple average of $\text{Re}[w_2]$ from the data points. This concludes the fitting procedure and establishes the full conformal map from z to w_2. It should be noted that the procedure described above is a self-contained new fitting method referred to as the conformal mapping (CM) method hereafter that applies to general S_{21} data at arbitrary power, provided that the off resonance point z_∞ is predetermined. Unlike the DCM methods, this procedure uses two linear fits instead of two nonlinear fits (circle fit and phase fit) which makes it simpler to implement. Furthermore, since z_∞ is assumed to be known, the method is best applied to data taken within one linewidth of f_r for the same reasons discussed earlier with regard to PC-DCM.

B. Direct mapping of the low power data

Using parameters extracted at high power, the full conformal map from S_{21} to w_2 is established as

$$w_2 = \frac{1}{1 - S_{21}\, e^{2j\pi f\tau}/z_\infty} \frac{e^{j\phi}}{Q_c} - \frac{\cos\phi}{Q_c}, \quad (11)$$

where the map is parameterized by τ, z_∞, Q_c, and ϕ. As discussed previously, these parameters are power independent. Once the map is established, it can be used to directly map any S_{21} data (measured at a single frequency or in a frequency span, on resonance or detuned from resonance) into w_2.

The conformal map provides a straightforward transformation of S_{21} data into $1/Q_i$ and $2\delta f/f_r$ values. According to Eq. (4), it is most efficient to measure S_{21} at a single frequency $f = f_r$ at lower powers, where f_r is the resonance frequency determined at high power in the linear regime, instead of performing a frequency sweep around f_r as is done in the DCM and PC-DCM. This is similar to other time-domain resonator measurement applications, such as kinetic inductance detectors and qubit readout, where the probe tone is fixed at the resonance frequency. The time-dependent single-frequency $S_{21}(t, f = f_r)$ data taken for a period of time T at each lower power are directly mapped to w_2-plane using Eq. (11). We plot these data as the colored dots in Figs. 3(a) and 3(c) alongside the high power data obtained from a frequency sweep. In Fig. 3(d), we plot extracted $1/Q_i$ values against $\langle n_{\text{ph}}\rangle$ generated from the mean of $\text{Re}[w_2]$ at each power with the error bar quoting the standard error of the mean. We hereafter refer to this method of directly mapping the single frequency $S_{21}(t)$ data to the w_2-plane to calculate $1/Q_i$ as the parameter-constrained conformal mapping (PC-CM) method. The ability to process lower power data without the need for any fitting is a unique feature of the PC-CM method and makes it advantageous over non-linear fitting because it is insensitive to choice of initial conditions or weighting of points.

V. RESULTS: COMPARING THE METHODS WITH EXPERIMENTAL DATA

We report comparison of the DCM, PC-DCM, CM, and PC-CM methods by analyzing experimental data on 100 nm evaporated Al and 100 nm sputtered Nb resonators on Si substrates. Each resonator chip has 12 $\lambda/4$ CPW resonators with designed resonance frequencies between 5.2 and 6.2 GHz and coupling $Q_c = 2 \times 10^6$. An electron micrograph of the fabricated resonator is shown in Fig. 1(a). The devices were cooled down in a dilution refrigerator or an adiabatic demagnetization refrigerator (ADR). Measurements were carried out using a VNA in a conventional cryogenic setup[4] shown in Fig. 4.

In the following discussions, unless otherwise noted, we always used the fitting results of DCM at the highest power to constrain the parameters in PC-DCM (Q_c, z_∞ and ϕ) and CM (z_∞ only). As for the PC-CM method, the lower power data were mapped to $1/Q_i$ using the conformal map established by a CM fit at the highest power. In addition, all error bars are quoted at the 68% confidence level (1σ).
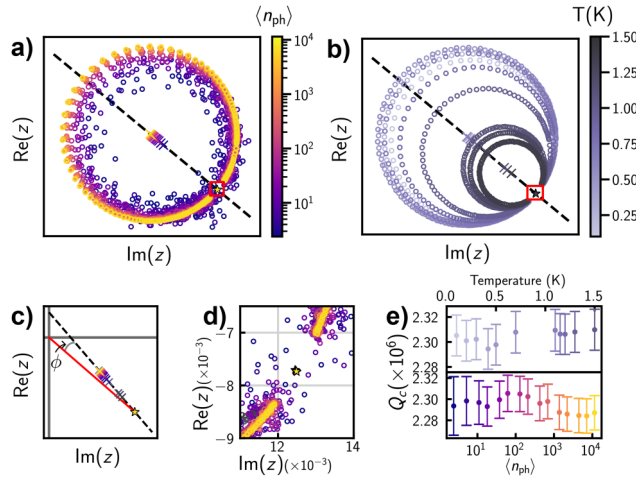
A. Validation of the power-independent assumption

The methods (PC-DCM, PC-CM) introduced here depend on the independence of the off resonance point z_∞, impedance mismatch angle ϕ, and coupling Q_c from the photon number $\langle n_{\text{ph}}\rangle$. Here we show that these three parameters are unchanged across a wide range of $\langle n_{\text{ph}}\rangle$ using data from a 100 nm Nb resonator measured in the ADR; we also show that these parameters are unchanged as a function of temperature for temperatures well below the critical temperature (9.2 K). We plot in Fig. 5(a) the power-dependent resonance curves measured at 300 mK and $\langle n_{\text{ph}}\rangle = 1 - 10^4$. In Fig. 5(b), we plot the temperature-dependent
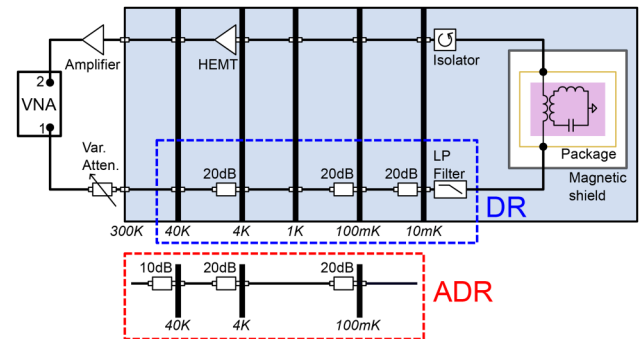
FIG. 4. Device and measurement setup. Two experimental setups were used in this study. A VNA was used to measure the S_{21} of a resonator in either a DR (dilution refrigerator) with a base temperature of 10 mK or ADR (adiabatic demagnetization refrigerator) with a variable temperature between 100 mK and 3 K. The input lines contained a series of attenuators for thermalization and to attenuate noise from higher temperature stages; blue (red) dashed boxes show the attenuator configurations for the DR (ADR). On the output side, two linear amplifiers including a HEMT were used to amplify the signal. A high permeability magnetic shield was used to reduce flux-trapping from stray fields.

FIG. 5. Validation of power-independent Q_c, ϕ, z_∞. (a) Resonance circles measured at 300 mK and $\langle n_{ph} \rangle = 1 - 10^4$. The fitted centers of the circles are marked by "×," which are then fit to a straight line (dashed line). The off-resonance points are marked by "★." (b) Resonance circles measured between 100 mK and 1.5 K at $\langle n_{ph} \rangle \sim 10^4$. (c) The circle centers of the power-dependent and temperature-dependent resonance circles plotted together. The corresponding linear fits are plotted as the dashed lines. The angle ϕ is formed between the dashed line and the red line that connects the off resonance point to the origin. (d) A combined zoomed-in plot of the red boxes in (a) and (b) showing the significant overlap of the power-dependent and temperature-dependent off resonance points. (e) The extracted Q_c values from PC-DCM fits on the power-dependent (bottom) and temperature-dependent (top) resonance circles.

resonance curves measured between 100 mK and 1.5 K at $\langle n_{ph} \rangle \sim 10^4$. All measurements used the same number of points, acquisition time, and frequency span.

We begin with an analysis of the power-dependent data. We determined the center of each resonance circle (marked by "×") with a circle fit. Next, we fit the center points to a straight line (dashed lines) with a slope of -0.8273 ± 0.0098 and an R^2 goodness-of-fit value of 0.998.[23] The fact that all the circle centers aligned along this common line indicates that the angle ϕ remained unchanged at different $\langle n_{ph} \rangle$. We then used the intersection of this line with the circle fits to determine the off resonance points (marked by "★") which we show in a close-up plot in Fig. 5(d). The large overlap of the points suggests that the off-resonance points also remained unchanged at different $\langle n_{ph} \rangle$. Finally, we used these values of ϕ and z_∞ to perform independent PC-DCM fits of all the resonance circles while allowing Q_c to vary. We plot the extracted Q_c values in Fig. 5(e). This analysis was repeated on the temperature-dependent resonance circles. The straight line fit of the circle centers in this case yielded a slope of -0.8293 ± 0.0048 and an R^2 goodness-of-fit value of 0.999. We plot the corresponding off resonance points and Q_c values in Figs. 5(d) and 5(e) which overlap well with the power-dependent results. Our results confirm that the resonator parameters z_∞, ϕ, and Q_c were unchanged when the internal loss changed in a wide range (whether due to TLS saturation or thermal quasi-particles). We note that it is good practice to

carry out this validation procedure to verify the power-independence assumption prior to using the parameter-constrained methods. Once confirmed, it is valid to treat these parameters as constant values, determine them from resonance circles measured at high power, and reuse them to fit data measured at lower powers.

B. Comparison of $1/Q_i$ in a full power sweep

In Fig. 6, we present data measured on a 100 nm Al resonator in the DR and compare the extracted $1/Q_i$ from each of the four methods as a function of $\langle n_{ph} \rangle$. We took three data sets in total. Each data set contained 100 data points with one set spanning six linewidths for DCM, another spanning one linewidth for PC-DCM and CM, and lastly a single frequency measurement for PC-CM, all centered around the resonance frequency. The same integration time per point was used for each data set.

We plot the extracted $1/Q_i$ against $\langle n_{ph} \rangle$ in Fig. 6(a). The error bars for DCM and PC-DCM were calculated from the covariance matrix of the fit while CM and PC-CM use the standard error of the mean as stated previously. The four methods give overall consistent curves that show $1/Q_i$ decreases with $\langle n_{ph} \rangle$ due to the TLS saturation effect. At $\langle n_{ph} \rangle \gg 1$ the $1/Q_i$ values agree well with each other to within 1% showing that they give equivalent results when the SNR is high. This implies that either DCM or CM can be used to determine the power-independent parameters at high power. At intermediate powers of $10 < \langle n_{ph} \rangle < 10^5$, the results from all four methods agree to within 6%. Finally in the single
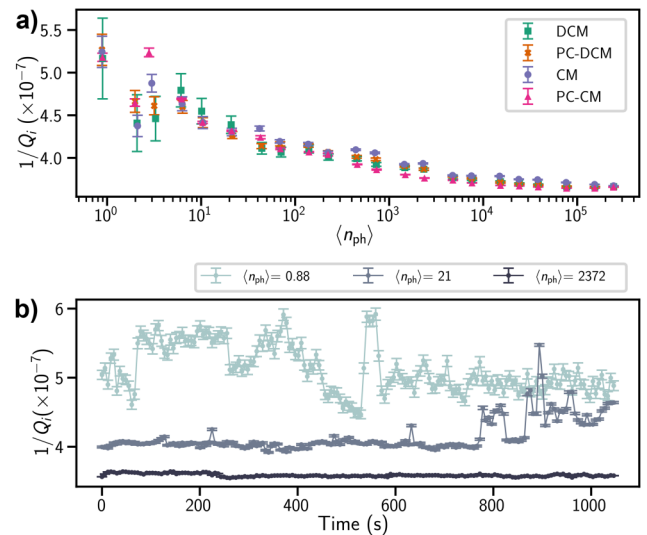
FIG. 6. Comparing $1/Q_i$ in a full power sweep using the same integration time per point. (a) $1/Q_i$ vs $\langle n_{ph} \rangle$ measured on a 100 nm Al resonator analyzed using the DCM, PC-DCM, CM, and PC-CM methods. (b) Time-dependent $1/Q_i$ values extracted using PC-CM at three different $\langle n_{ph} \rangle$. In the $\langle n_{ph} \rangle \approx 1$ case, the drift of $1/Q_i$ over time is larger than the error bars produced by PC-CM. This showcases that at low powers the uncertainty in $1/Q_i$ is dominated by the intrinsic fluctuations of the resonator due to TLS and less so by the measurement hardware noise (amplifier noise).

photon regime ($\langle n_{\mathrm{ph}} \rangle \sim 1$), we begin to see large deviations over 10%. There are two main contributions that factor into the deviations: the fitting uncertainty from the HEMT (high electron mobility transistor) noise and the TLS-induced fluctuations. Superconducting CPW resonators are known to fluctuate in quality factor as a result of two-level systems. Changes of up to 30% within tens of minutes have been observed in the literature.[24–26] In our case, the third single frequency data set was taken several minutes after the first data set. Also, the error bars reported in Fig. 6(a) only account for the measurement white noise and do not factor in TLS-induced fluctuations.

We further explored these TLS-induced fluctuations by measuring single frequency data spanning a period of 1000 s at three power levels and processed the data using the PC-CM method. We plot the resulting $1/Q_i$ against time in Fig. 6(c). Each data point is the average of 575 $1/Q_i$ values measured in 5.75 s with the error bars quoting the standard error of the mean. We confirm that the internal loss is capable of changing by 30% or more within minutes at $\langle n_{\mathrm{ph}} \rangle \sim 1$. In addition, we also found the magnitude of fluctuations decreased with increasing $\langle n_{\mathrm{ph}} \rangle$ as expected from TLS saturation. While a discussion of the rich physics behind these observations is beyond the scope of this methodology-focused paper, we have demonstrated that the presented non-conventional single-frequency measurement and conformal mapping data analysis techniques are useful tools to study these phenomena.

C. Comparison of fitting uncertainties

An additional feature we see in Fig. 6 is that the error bars at any $\langle n_{\mathrm{ph}} \rangle$ are different and in a fixed order (largest for DCM and smallest for PC-CM). Here we take a closer look at the errors (uncertainty) in the extracted $1/Q_i$ by measuring a 100 nm Nb resonator in the ADR and compare the errors reported by each of the fitting methods. Four data sets were measured in total. We took one frequency sweep that spanned 3 linewidths for DCM, one that spanned 1 linewidth for PC-DCM and CM, and a single frequency measurement for PC-CM. The fourth data set was also a single frequency measurement that was taken off resonance (2 MHz de-tuned from the resonance) to assess the measurement noise.

We plot the extracted $1/Q_i$ vs $\langle n_{\mathrm{ph}} \rangle$ in Fig. 7(a). The results from the four methods agree with each other with a maximum difference of 1.1% occurring at the lowest $\langle n_{\mathrm{ph}} \rangle \sim 1000$. Fit quality was evaluated by calculating the reduced chi-square χ_ν^2 statistic and we plot the results in Fig. 7(c). We find an average $\langle \chi_\nu^2 \rangle \sim 1.28$ across all $\langle n_{\mathrm{ph}} \rangle$. However, the different methods yielded different standard errors in $1/Q_i$ as shown in Fig. 7(b). Two clear trends can be observed in the data. First, the errors all scale inversely with the photon number as expected from the reduced SNR at lower powers. Second, at any photon number the errors follow the order $\sigma_{\mathrm{DCM}} > \sigma_{\mathrm{PC-DCM}} \approx \sigma_{\mathrm{CM}} > \sigma_{\mathrm{PC-CM}}$, showing that PC-DCM, CM, and PC-CM achieve lower error than the conventional DCM with PC-CM showing the lowest error. This second trend is consistent with our intuition that data taken closer to (further away from) the resonance contains more (less) information about the properties of the resonator and should result in better (worse) estimates of $1/Q_i$. Therefore, it is unsurprising that the different frequency spans used by the four methods resulted in different fitting uncertainties.
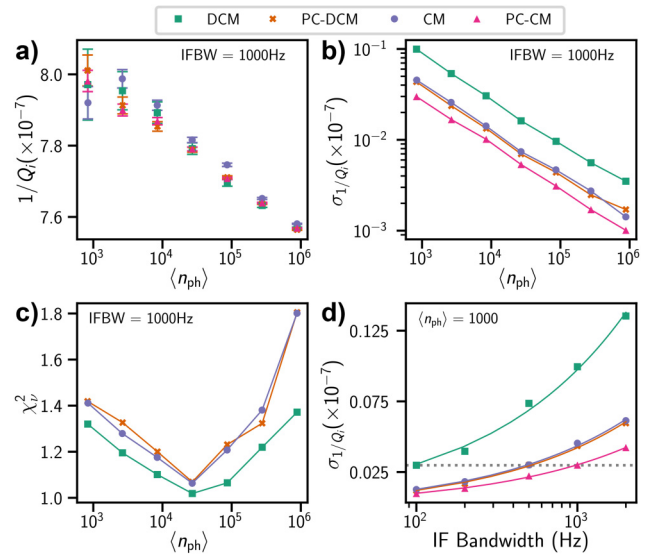
FIG. 7. Comparison of fitting uncertainties from the four methods. The data shown is for a 100 nm Nb resonator measured in the ADR at 1 K. (a) $1/Q_i$ vs $\langle n_{\mathrm{ph}} \rangle$ as determined by each of the four methods for data measured using a VNA IFBW of 1000 Hz. (b) Errors in $1/Q_i$ reported by each method against $\langle n_{\mathrm{ph}} \rangle$. The errors for DCM and PC-DCM were found from the covariance matrix while the standard errors for CM and PC-CM methods were directly calculated in the w_2 plane (see Fig. 3) from the standard error of the mean: $\sqrt{\mathrm{Var}(\mathrm{Re}[w_2])/(N-1)}$ where $N = 200$ is the number of data points. These are also plotted as error bars in (a). (c) The reduced χ_ν^2 vs $\langle n_{\mathrm{ph}} \rangle$ corresponding to each of the fits in (a,b). In order to calculate χ_ν^2 we estimated the measurement noise by calculating the variance of the transmission background as $\sigma_z^2 = \mathrm{Var}[S_{21}(f^*) e^{j2\pi f^* \tau}]$, where $S_{21}(f^*)$ are data points measured at a single frequency $f^* = f_r + 2$ MHz far off resonance. The small increase of χ_ν^2 over 1 at high power (low power) end is likely due to excess noise from saturated TLS[21,24,25] (long-term fluctuations from unsaturated TLS discussed earlier in this paper). (d). The standard errors in $1/Q_i$ reported by each method for data taken at $\langle n_{\mathrm{photon}} \rangle = 1000$ vs VNA IFBW. The solid lines correspond to best fits to the scaling law $\sigma_{1/Q_i} \propto \sqrt{\mathrm{IFBW}}$.

The ratios of uncertainties in $1/Q_i$ from the four methods at each $\langle n_{\mathrm{ph}} \rangle$ [Fig. 7(b)] is found to be $\sigma_{\mathrm{DCM}} : \sigma_{\mathrm{PC-DCM}} (\sigma_{\mathrm{CM}}) : \sigma_{\mathrm{PC-CM}} \approx 3.5 : 1.5 (1.5) : 1$. Because the measurement time to achieve a given uncertainty level in $1/Q_i$ scales as $1/\sigma^2$, we expect that the PC-CM and CM (PC-DCM) methods can reduce the measurement time by a factor of 10 and 5 (5), respectively, as compared to the conventional DCM. To demonstrate this measurement time reduction advantage, we measured additional data sets at $\langle n_{\mathrm{ph}} \rangle = 1000$ with the same 200 data points but used different VNA IF bandwidths (IFBW) from 2000 Hz down to 100 Hz. This corresponded to measurement times from 0.1 to 2 s. The errors in $1/Q_i$ against IFBW are plotted in Fig. 7(d). We find that the standard error achieved by PC-CM (CM and PC-DCM) at an IFBW of 1000 Hz (500 Hz) is comparable to the one given by DCM at an IFBW of 100 Hz (dashed line), which indeed translates into a factor 10 (5) reduction in measurement time for the PC-CM (CM and PC-DCM) from the conventional DCM. In addition, we find that the error in Fig. 7(d) for each method scales as the

square-root of the IFBW. This suggests the measurement is dominated by the white noise from our HEMT which has an input-referred noise temperature of 5 K. This showcases that the new methods are able to improve measurement uncertainty or efficiency over the conventional diameter correction method in the presence of white noise. In addition, the decreased measurement times of the PC-DCM and PC-CM should also help to reduce fitting errors due to TLS-induced fluctuations.

VI. DISCUSSION AND CONCLUSION

As we have discussed in the previous section, there are two main noise sources that contribute to the uncertainty in the extracted $1/Q_i$ measured in the single photon regime: amplifier noise and the intrinsic TLS-induced fluctuations. Our proposed methods (PC-DCM and PC-CM) address the first contribution and improve the fitting uncertainty by focusing the measurement to be at or very close to the resonance frequency where the S_{21} is most sensitive to the underlying parameter $1/Q_i$. We remark that this is only possible by constraining parameters because the conventional unconstrained DCM requires data away from resonance by necessity in order to fit the resonance circle and extract values for z_∞, ϕ, and Q_c. We also note that these new methods are equally applicable to both HEMT or parametric amplifiers with quantum limited noise. Our new methods do not address the noise contribution from the intrinsic TLS-induced fluctuations but provide a useful tool to study this phenomenon. In particular, PC-CM can be used to measure changes in the resonator frequency by reading the fractional frequency shift from the imaginary part of w_2.

Two additional considerations should be noted when applying the new analysis techniques. First, the single measurement frequency f used in the PC-CM method should be set as close as possible to the resonance frequency f_r, but a small detuning or drift in f_r is tolerable. This is because the conformal map defined in Eq. (11) is valid for any frequency on or off resonance, assuming Eq. (1) accurately describes the S_{21} response of the resonator. The conformal map separates changes in f_r and $1/Q_i$ into two orthogonal directions so that drift in f_r corresponds to movement only along the imaginary axis in the w_2 plane without any changes in the $1/Q_i$ value; this also suggests that the $1/Q_i$ value extracted using PC-CM is insensitive to frequency noise. As a rule of thumb, we recommend to always keep f to within one linewidth of f_r at all times when applying PC-CM. Second, the new analysis techniques have been successfully applied to Nb and Al resonators with low kinetic inductance fractions, but special care should be taken when applying our technique to resonators fabricated from materials with high kinetic inductance, such as TiN or NbTiN. One should avoid using these techniques in the high power, non-linear regime where the resonance circles are distorted and Eq. (1) is no longer valid in describing the S_{21} response. Any fitting or mapping should be done in the linear regime, which applies in general to measurement near the single-photon level.

In conclusion, we presented new measurement and data analysis methods for resonator internal loss that are more accurate, efficient, and robust than the conventional diameter correction method. Extracting a subset of power-independent resonator parameters from high power enabled us to spend measurement time more efficiently on resonance to reduce the fitting uncertainty as we have shown

with experimental data. In particular, the conformal mapping method provides an efficient way to analyze transmission data gathered on resonators by directly mapping S_{21} data into $1/Q_i$ and $2\delta f/f_r$ values. All together, these new resonator loss measurements extend the toolbox available to experimentalists for studying the physical origins of dissipation, noise and decoherence in quantum circuits as well as to characterize materials used for quantum devices.

AUTHOR DECLARATIONS

Conflict of Interest

The authors have no conflicts to disclose.

Author Contributions

C.C. and D.P. contributed equally to this work.

Cliff Chen: Data curation (equal); Formal analysis (equal); Investigation (equal); Software (equal); Writing – original draft (equal); Writing – review & editing (equal). **David Perello:** Data curation (equal); Formal analysis (equal); Investigation (equal); Writing – original draft (equal); Writing – review & editing (equal). **Shahriar Aghaeimeibodi:** Methodology (supporting); Software (supporting). **Guillaume Marcaud:** Methodology (supporting). **Ignace Jarrige:** Methodology (supporting). **Hanho Lee:** Investigation (supporting). **Warren Fon:** Investigation (supporting). **Matt Matheny:** Conceptualization (equal); Project administration (equal); Resources (equal); Writing – review & editing (equal). **Jiansong Gao:** Conceptualization (equal); Formal analysis (equal); Investigation (equal); Methodology (equal); Supervision (equal); Writing – original draft (equal); Writing – review & editing (equal).

DATA AVAILABILITY

The data that support the findings of this study are available from the corresponding author upon reasonable request.

REFERENCES

[1] A. Wallraff, D. I. Schuster, A. Blais, L. Frunzio, R.-S. Huang, J. Majer, S. Kumar, S. M. Girvin, and R. J. Schoelkopf, "Strong coupling of a single photon to a superconducting qubit using circuit quantum electrodynamics," Nature **431**, 162 (2004).

[2] J. Koch, T. M. Yu, J. Gambetta, A. A. Houck, D. I. Schuster, J. Majer, A. Blais, M. H. Devoret, S. M. Girvin, and R. J. Schoelkopf, "Charge-insensitive qubit design derived from the cooper pair box," Phys. Rev. A **76**, 042319 (2007).

[3] J. A. Schreier, A. A. Houck, J. Koch, D. I. Schuster, B. R. Johnson, J. M. Chow, J. M. Gambetta, J. Majer, L. Frunzio, M. H. Devoret, S. M. Girvin, and R. J. Schoelkopf, "Suppressing charge noise decoherence in superconducting charge qubits," Phys. Rev. B **77**, 180502 (2008).

[4]C. R. H. McRae, H. Wang, J. Gao, M. R. Vissers, T. Brecht, A. Dunsworth, D. P. Pappas, and J. Mutus, "Materials loss measurements using superconducting microwave resonators," Rev. Sci. Instrum. **91**, 091101 (2020).

[5]A. Bilmes, A. K. Händel, S. Volosheniuk, A. V. Ustinov, and J. Lisenfeld, "*In-situ* bandaged Josephson junctions for superconducting quantum processors," Supercond. Sci. Technol. **34**, 125011 (2021).

[6]T. Lindström, J. E. Healey, M. S. Colclough, C. M. Muirhead, and A. Y. Tzalenchuk, "Properties of superconducting planar resonators at millikelvin temperatures," Phys. Rev. B **80**, 132501 (2009).

[7]P. Macha, S. H. W. van der Ploeg, G. Oelsner, E. Il'ichev, H.-G. Meyer, S. Wünsch, and M. Siegel, "Losses in coplanar waveguide resonators at millikelvin temperatures," Appl. Phys. Lett. **96**, 062503 (2010).

[8]P. W. Anderson, B. I. Halperin, and C. M. Vama, "Anomalous low-temperature thermal properties of glasses and spin glasses," Philos. Mag. **25**(1), 1–9 (1972).

[9]W. A. Phillips, "Two-level states in glasses," Rep. Prog. Phys. **50**, 1657 (1987).

[10]D. S. Wisbey, J. Gao, M. R. Vissers, F. C. S. da Silva, J. S. Kline, L. Vale, and D. P. Pappas, "Effect of metal/substrate interfaces on radio-frequency loss in superconducting coplanar waveguides," J. Appl. Phys. **108**, 093918 (2010).

[11]M. S. Khalil, F. C. Wellstood, and K. D. Osborn, "Loss dependence on geometry and applied power in superconducting coplanar resonators," IEEE Trans. Appl. Supercond. **21**(3), 879–882 (2011).

[12]J. M. Sage, V. Bolkhovsky, W. D. Oliver, B. Turek, and P. B. Welander, "Study of loss in superconducting coplanar waveguide resonators," J. Appl. Phys. **109**, 063915 (2011).

[13]L. Faoro and L. B. Ioffe, "Internal loss of superconducting resonators induced by interacting two-level systems," Phys. Rev. Lett. **109**, 157005 (2012).

[14]P. G. Baity, C. Maclean, V. Seferai, J. Bronstein, Y. Shu, T. Hemakumara, and M. Weides, "Circle fit optimization for resonator quality factor measurements: Point redistribution for maximal accuracy," Phys. Rev. Res. **6**, 013329 (2024).

[15]S. Probst, F. B. Song, P. A. Bushev, A. V. Ustinov, and M. Weides, "Efficient and robust analysis of complex scattering data under noise in microwave resonators," Rev. Sci. Instrum. **86**, 024706 (2015).

[16]J. Gao, "The physics of superconducting resonators," Ph.D thesis (Caltech, Pasadena, CA, 2008).

[17]M. S. Khalil, M. J. A. Stoutimore, F. C. Wellstood, and K. D. Osborn, "An analysis method for asymmetric resonator transmission applied to superconducting devices," J. Appl. Phys. **111**, 054510 (2012).

[18]H. Guan, M. Dai, Q. He, J. Hu, P. Ouyang, Y. Wang, L. F. Wei, and J. Gao, "Network modeling of non-ideal superconducting resonator circuits," Supercond. Sci. Technol. **33**, 075004 (2020).

[19]J. Zmuidzinas, "Superconducting microresonators: Physics and applications," Annu. Rev. Condens. Matter Phys. **3**, 169–214 (2012).

[20]R. E. Collin, *Foundations for Microwave Engineering* (Wiley, 2001).

[21]J. Gao, L. R. Vale, J. A. B. Mates, D. R. Schmidt, G. C. Hilton, K. D. Irwin, F. Mallet, M. A. Castellanos-Beltran, K. W. Lehnert, J. Zmuidzinas, and H. G. Leduc, "Strongly quadrature-dependent noise in superconducting microresonators measured at the vacuum-noise limit," Appl. Phys. Lett. **98**, 232508 (2011).

[22]D. N. Arnold and J. Rogness, "Möbius transformations revealed," Not. AMS **55**, 1226 (2008).

[23]J. L. Devore, *Probability and Statistics for Engineering and the Sciences* (Cengage Learning, Boston, 2011).

[24]J. Béjanin, Y. Ayadi, X. Xu, C. Zhu, H. Mohebbi, and M. Mariantoni, "Fluctuation spectroscopy of two-level systems in superconducting resonators," Phys. Rev. Appl. **18**, 034009 (2022).

[25]C. T. Earnest, J. H. Béjanin, T. G. McConkey, E. A. Peters, A. Korinek, H. Yuan, and M. Mariantoni, "Substrate surface engineering for high-quality silicon/aluminum superconducting resonators," Supercond. Sci. Technol. **31**, 125013 (2018).

[26]A. Vallières, M. E. Russell, X. You, D. A. Garcia-Wetten, D. P. Goronzy, M. J. Walker, M. J. Bedzyk, M. C. Hersam, A. Romanenko, Y. Lu, A. Grassellino, J. Koch, and C. R. H. McRae, "Loss tangent fluctuations due to two-level systems in superconducting microwave resonators" (2024).

20 February 2025 03:25:50